A Two-Stage Color Image Segmentation Method Based on Saturation-Value Total Variation

Tiange Wang* and Hok Shing Wong

Department of Mathematics, The Chinese University of Hong Kong, Hong Kong

Abstract. Color image segmentation is crucial in image processing and computer vision. Most traditional segmentation methods simply regard an RGB color image as the direct combination of the three monochrome images and ignore the inherent color structures within channels, which contain some key feature information of the image. To better describe the relationship of color channels, we introduce a quaternion-based regularization that can reflect the image characteristics more intuitively. Our model combines the idea of the Mumford-Shah model-based two-stage segmentation method and the Saturation-Value Total Variation regularization for color image segmentation. The new strategy first extracts features from the color image and then subdivides the image in a new color feature space which achieves better performance than methods in RGB color space. Moreover, to accelerate the optimization process, we use a new primal-dual algorithm to solve our novel model. Numerical results demonstrate clearly that the performance of our proposed method is excellent.

1 Introduction

Color image segmentation is an important and challenging task in image processing and computer vision. The goal of image segmentation is to divide an image into different parts with similar characteristics. This process has vast applications in many fields, such as biomedical imaging [44], object detection [23, 50], and astronomical imaging [41], etc. In the literature, many excellent methods have been proposed for image segmentation [37, 39, 40, 49, 54]. One of the most effective and significant segmentation models is

---

*Corresponding author.
Emails: tgwang@math.cuhk.edu.hk (T. Wang), hswong@math.cuhk.edu.hk (H. Wong)

the Mumford-Shah model (MS) [40]. Let $\Omega \subset \mathbb{R}^2$ be a bounded open connected set, and Γ be a compact curve in Ω, the MS model can be formulated as

$$E_{\text{MS}}(u, \Gamma; \Omega) = \frac{\lambda}{2} \int_\Omega (f-u)^2 dx + \frac{\mu}{2} \int_{\Omega \backslash \Gamma} |\nabla u|^2 dx + \text{Length}(\Gamma), \qquad (1.1)$$

where λ, μ are positive parameters, $f : \Omega \to \mathbb{R}$ is the degraded image and $u : \Omega \to \mathbb{R}$ is the ideal image. Here the length of Γ can also be written as $\mathcal{H}^1(\Gamma)$, i.e., the 1-dimensional Hausdorff measure in $\mathbb{R}^2$. It is challenging to approximate the solution of Model (1.1) since it is a nonconvex minimization problem.

Over the years, plenty of methods [1,2,11,12,25,38] have been proposed to minimize or approximate the Mumford–Shah energy (1.1). Meanwhile, in order to overcome the computational complexity, numerous models and approaches related to the Mumford-Shah Model are proposed, such as the famous Chan-Vese Model [16], convex relaxation approaches [6,15,42] and multiphase segmentation algorithms [3,7,22,33,35,54], etc. In [10], a two-stage image segmentation strategy for gray-scale images was proposed and it performed well on the segmentation task. For this method, the first stage is to find a smooth image u by minimizing the following energy:

$$\inf_u \left\{ \frac{\lambda}{2} \int_\Omega (f - \mathcal{A}u)^2 dx + \frac{\mu}{2} \int_\Omega |\nabla u|^2 dx + \int_\Omega |\nabla u| dx \right\}, \qquad (1.2)$$

where $\mathcal{A}$ can be the identity operator for noisy observed image f or a blurring operator for the blurred case. Then the second stage is to segment by thresholding u properly. Base on the two-stage idea, many novel image segmentation methods [14,20,24,34,51] have been proposed. They show the close correlation between image restoration and segmentation to some extent and all these two-stage methods have achieved good results in image segmentation.

Conceiving an effective color image segmentation method is not a simple extension of approaches for gray images, because both the brightness and chrominance information need to be considered. Most methods are proposed in the usual RGB color space [8,30, 43,46], but it has been observed that the RGB color space is not suitable for segmentation since it often fails to reflect features of real-world color images due to the lack of correlation between the three channels of RGB space. In [45], RGB image is converted to the HSI (Hue, Saturation and Intensity) color space for segmentation. In [4], a segmentation method for grayscale images is extended to color images in RGB, HSV (hue, saturation and value) and CB (chroma-brightness) color spaces. It shows that color image in the HSV color spaces is similar to human color perception, and seems to be grouped more easily than in RGB color space (see Fig. 2 for illustration). In this paper, we will further showcase through experiments that image segmentation using features in the HSV space is valid and effective.

An effective way to represent color images is to use quaternions. Many previous works [18,19,52,53] employ quaternions to express the color images. Among these
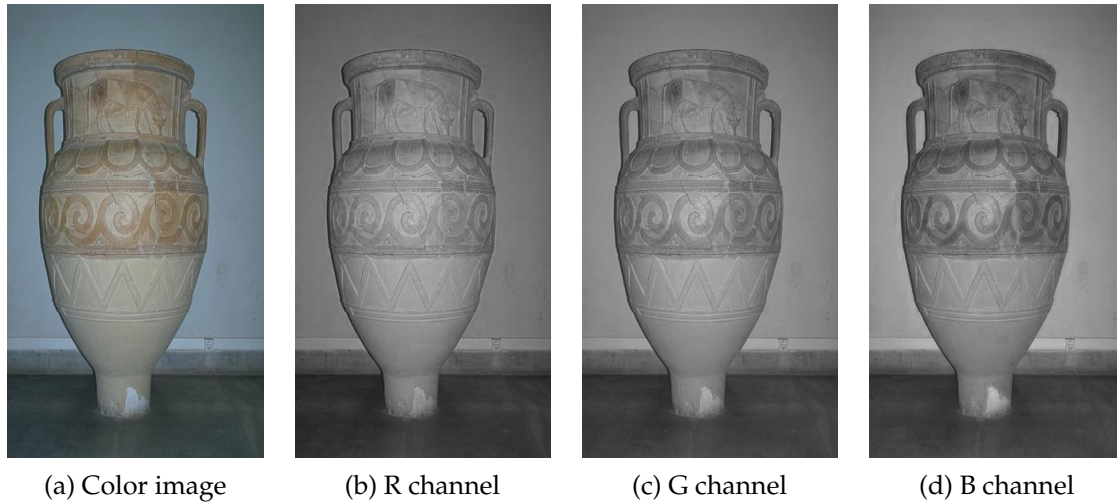
| (a) Color image | (b) R channel | (c) G channel | (d) B channel |

Figure 1: From left to right: the color image, the red channel image, the green channel image, and the blue channel image.

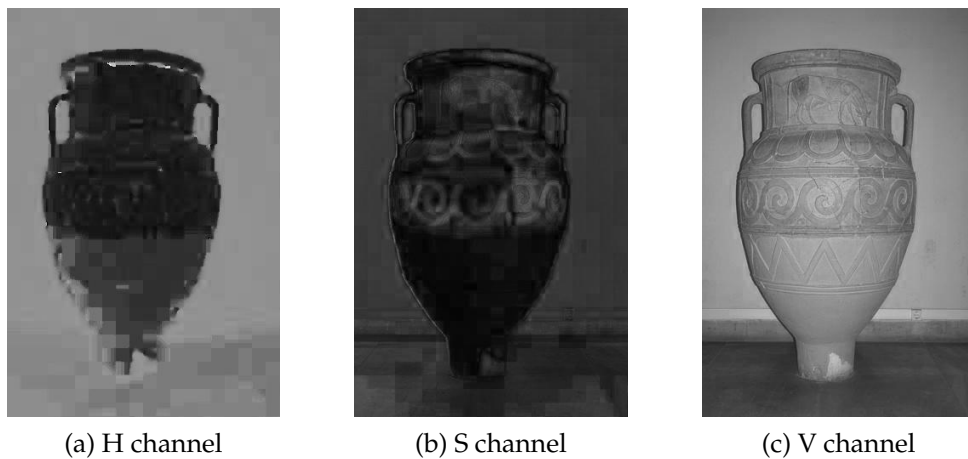

| (a) H channel | (b) S channel | (c) V channel |

Figure 2: From left to right: the H channel image, the S channel image, the V channel image.

works, [52] apply the dictionary learning algorithm with quaternions for color image restoration. They achieve good results by representing color images with the quaternion matrix and transform their model into the quaternion domain. The quaternions have been successfully applied in many color image processing problems [17,55] by using the quaternion matrix representation. In [29], Jia et al. proposed a new saturation-value color total variation regularization to restore color image in the HSV color space instead of in the original RGB color space. As the quaternions can easily represent spatial orientations and rotations of elements in three-dimensional space, we believe that representing color images by quaternions can intuitively reflect the structural information between channels

and is better than simply treat RGB channels as three independent monochrome images.

In this paper, we propose a novel two-stage color image segmentation method based on the SV-TV regularization. We transform the quaternion-represented color image into the HSV space to construct a new regularization that focuses on the characteristics of saturation and value and then propose our two-stage segmentation model based on this regularization. In the first stage, we represent the color image with a feature extraction matrix and find a smooth approximation in the color feature domain directly. Followed by that, we segment the image by thresholding the smooth approximation into different parts in the second stage. The main contributions of our method are as follows:

- Different from the conventional color image segmentation methods, which treat the RGB color image as three independent monochrome images, we consider the intrinsic connection between multiple channels by introducing the SV-TV regularization into our model, which reflects that our model considers not only color information in the RGB space, but also lightness and saturation information in the HSV space.

- We propose an effective two-stage segmentation model based on the SV-TV regularization for degraded color image (with noise, blur, and missing pixels), and it overcomes the shortcomings of other traditional segmentation methods that are less effective in the case of image degradation.

- For the numerical implementation, we design the iterative scheme through a novel first-order primal-dual algorithm with guaranteed convergence.

The rest of the paper is organized as follows. In Section 2, we review the basic concepts of the quaternions and the SV-TV regularization. We elaborate on our new method and carefully apply the first-order primal-dual algorithm to solve the optimization model in Section 3. Experimental results are in Sectionc4. Finally, the conclusion follows in Section 5.

2 Quaternion and SV-TV regularization

2.1 Quaternion

Quaternion was first described by Hamilton [26], and recently it is widely used in image processing as representing color images with quaternions can better preserve the inherent connection between multiple channels [17]. A function $\mathbf{u}(x,y)$ on Ω is defined as

$$\mathbf{u}(x,y) = u_0(x,y) + u_1(x,y)\mathbf{i} + u_2(x,y)\mathbf{j} + u_3(x,y)\mathbf{k}, \tag{2.1}$$

where $(x,y) \in \Omega$, $u_0(x,y), u_1(x,y), u_2(x,y), u_3(x,y) \in \mathbb{R}$ and $\mathbf{i}$, $\mathbf{j}$, $\mathbf{k}$ are imaginary units satisfying

$$\mathbf{i}^2 = \mathbf{j}^2 = \mathbf{k}^2 = \mathbf{ijk} = -1.$$

For a RGB color image $\mathbf{u}(x,y)$, we can represent it by a pure quaternion, i.e., $u_0(x,y)$ is always 0:

$$\mathbf{u}(x,y) = u_r(x,y)\mathbf{i} + u_g(x,y)\mathbf{j} + u_b(x,y)\mathbf{k}, \tag{2.2}$$

here (x,y) is the pixel location of a color image $\mathbf{u}$, and $u_r(x,y)$, $u_g(x,y)$, $u_b(x,y)$ are the red, green, and blue (RGB) channels, respectively. The magnitude of $\mathbf{u}(x,y)$ is defined by

$$|\mathbf{u}(x,y)| = \sqrt{u_r(x,y)^2 + u_g(x,y)^2 + u_b(x,y)^2}.$$

2.2 HSV color space and SV-TV regularization

Introduced by [19], a quaternion-represented RGB image $\mathbf{u}(x,y)$ described in (2.2) can be transformed into HSV components (denoted by u_h, u_s, u_v, respectively) using quaternion operations:

$$\begin{cases} u_h(x,y) = \tan^{-1}\left(\dfrac{|\mathbf{u}(x,y) - \boldsymbol{\mu}\boldsymbol{\nu}\mathbf{u}(x,y)\boldsymbol{\nu}\boldsymbol{\mu}|}{|\mathbf{u}(x,y) - \boldsymbol{\nu}\mathbf{u}(x,y)\boldsymbol{\nu}|} \right), \\[2mm] u_s(x,y) = \dfrac{1}{2}|\mathbf{u}(x,y) + \boldsymbol{\mu}\mathbf{u}(x,y)\boldsymbol{\mu}|, \\[2mm] u_v(x,y) = \dfrac{1}{2}|\mathbf{u}(x,y) - \boldsymbol{\mu}\mathbf{u}(x,y)\boldsymbol{\mu}|, \end{cases}$$

where $\boldsymbol{\mu} = \frac{1}{\sqrt{3}}(\mathbf{i}+\mathbf{j}+\mathbf{k})$ is referred to as the gray-value axis, and $\boldsymbol{\nu}$ is an unit and pure quaternion which is orthogonal to $\boldsymbol{\mu}$. Here i, j, k denote the imaginary units of a quaternion and correspond to R, G, B channels respectively in the case of an image. According to the algebra of quaternions, we have

$$u_s(x,y) = \frac{1}{3}\left\| C\mathbf{u}(x,y)^T \right\|_2, \quad u_v(x,y) = \frac{1}{\sqrt{3}}\left|u_r(x,y) + u_g(x,y) + u_b(x,y)\right|, \tag{2.3}$$

where

$$\mathbf{C} = \begin{bmatrix} 2 & -1 & -1 \\ -1 & 2 & -1 \\ -1 & -1 & 2 \end{bmatrix}, \quad \mathbf{u}(x,y)^T = \begin{bmatrix} u_r(x,y) \\ u_g(x,y) \\ u_b(x,y) \end{bmatrix}.$$

As introduced by Jia et al. [29], we can then define the total variation for saturation channel and value channel by defining the following norm:

$$|(\nabla_x\mathbf{u})_{ij}|_s = \frac{1}{3}\|\mathbf{C}(\nabla_x\mathbf{u})_{ij}\|_2, \tag{2.4a}$$

$$|(\nabla_y\mathbf{u})_{ij}|_s = \frac{1}{3}\|\mathbf{C}(\nabla_y\mathbf{u})_{ij}\|_2, \tag{2.4b}$$

$$|(\nabla_x\mathbf{u})_{ij}|_v = \frac{1}{\sqrt{3}}|(\nabla_x\mathbf{u}_r)_{ij} + (\nabla_x\mathbf{u}_g)_{ij} + (\nabla_x\mathbf{u}_b)_{ij}|, \tag{2.4c}$$

$$|(\nabla_y\mathbf{u})_{ij}|_v = \frac{1}{\sqrt{3}}|(\nabla_y\mathbf{u}_r)_{ij} + (\nabla_y\mathbf{u}_g)_{ij} + (\nabla_y\mathbf{u}_b)_{ij}|, \tag{2.4d}$$

here we use the first-order backward difference operator with the periodic boundary condition, i.e., $\nabla \mathbf{u} = (\nabla_x \mathbf{u}, \nabla_y \mathbf{u})$ is defined as

$$(\nabla_x \mathbf{u})_{ij} = \begin{cases} \mathbf{u}(i,j) - \mathbf{u}(i-1,j), & \text{if } 1 < i \leq M, \quad 1 \leq j \leq N, \\ \mathbf{u}(i,j) - \mathbf{u}(M,j), & \text{if } i = 1, \qquad 1 \leq j \leq N, \end{cases}$$

$$(\nabla_y \mathbf{u})_{ij} = \begin{cases} \mathbf{u}(i,j) - \mathbf{u}(i,j-1), & \text{if } 1 \leq i \leq M, \quad 1 < j \leq N, \\ \mathbf{u}(i,j) - \mathbf{u}(i,N), & \text{if } 1 \leq i \leq M, \quad j = 1. \end{cases}$$

Then the SV-TV regularization is expressed as:

$$\text{SV-TV}(\mathbf{u}) = \sum_{i=1}^{m} \sum_{j=1}^{n} \left(\sqrt{|(\nabla_x \mathbf{u})_{ij}|_s^2 + |(\nabla_y \mathbf{u})_{ij}|_s^2} + \alpha \sqrt{|(\nabla_x \mathbf{u})_{ij}|_v^2 + |(\nabla_y \mathbf{u})_{ij}|_v^2} \right), \qquad (2.5)$$

where $\alpha > 0$ is the weight of the value component.

To simplify the notations, we let $\mathbf{C} = \mathbf{P}^T \mathbf{Q} \mathbf{P}$, where

$$\mathbf{P} = \begin{bmatrix} \dfrac{1}{\sqrt{2}} & \dfrac{-1}{\sqrt{2}} & 0 \\ \dfrac{1}{\sqrt{6}} & \dfrac{1}{\sqrt{6}} & \dfrac{-2}{\sqrt{6}} \\ \dfrac{1}{\sqrt{3}} & \dfrac{1}{\sqrt{3}} & \dfrac{1}{\sqrt{3}} \end{bmatrix}, \quad \mathbf{Q} = \begin{bmatrix} 3 & 0 & 0 \\ 0 & 3 & 0 \\ 0 & 0 & 0 \end{bmatrix}. \qquad (2.6)$$

We further define

$$\hat{\mathbf{P}} = \mathbf{P} \otimes \mathbf{I}, \qquad (2.7)$$

where $\mathbf{I}$ is the identity matrix of appropriate size and denote

$$\begin{bmatrix} q_1(i,j) \\ q_2(i,j) \\ q_3(i,j) \end{bmatrix} = \hat{\mathbf{P}} \begin{bmatrix} u_r(i,j) \\ u_g(i,j) \\ u_b(i,j) \end{bmatrix}.$$

Then the SV-TV($\mathbf{u}$) can be rewritten as the following form

$$\text{SV-TV}(\mathbf{u})$$

$$= \sum_{i=1}^{m} \sum_{j=1}^{n} \left(\sqrt{\sum_{k=1}^{2} (\nabla_x q_k(i,j))^2 + (\nabla_y q_k(i,j))^2} + \alpha \sqrt{(\nabla_x q_3(i,j))^2 + (\nabla_y q_3(i,j))^2} \right). \qquad (2.8)$$

In (2.8), the SV-TV regularization is transformed to some normal total variation terms after applying the transformation matrix $\hat{\mathbf{P}}$ on $\mathbf{u}$, which indicates that $\hat{\mathbf{P}}$ plays an important role. The SV-TV regularization takes into account the saturation and brightness information of the image, which shows that the transformation $\hat{\mathbf{P}}$ can effectively extract these two types of image characteristics. Thus in our model, we first apply the $\hat{\mathbf{P}}$-transform on the given image, which not only can simplify our model but more significantly, allows us to use more image features than just the image color information for segmentation. The experiments show that using the SV-TV and performing $\hat{\mathbf{P}}$ matrix operation can overcome the shortcomings of a segmentation method that uses only RGB color information.

3   Proposed model

3.1   Two-stage SV-TV regularized segmentation

In this paper, we propose a two-stage segmentation method based on Saturation-Value Total Variation regularization. Similar to other two-stage methods' structure, the flow of our method can be concluded as Fig. 3. Cai et al. [10] proposed a Mumford-Shah Model-based method combining with total variation regularization (1.2) for smoothing the gray image in the first stage and have achieved good results. For color image segmentation, Cai et al. [9] add an extra step to transform the smoothed RGB color image to the LAB color space after the first stage through their SLaT Method. It is very effective for color segmentation because images in the LAB color space contain some relationships among the RGB channels. Motivated by this idea, to preserve the structure of a color image and extract more features, we apply the quaternion-based SV-TV regularization in the first stage of our model. Combining with the Mumford-Shah model-based method (1.2), our novel proposed model can be formulated as:

$$\min_{\mathbf{u}} \frac{\lambda}{2}\|\mathbf{f}-\mathcal{A}\mathbf{u}\|_2^2+\frac{\mu}{2}\|\nabla\mathbf{u}\|_2^2+\text{SV-TV}(\mathbf{u}), \tag{3.1}$$

where $\mathcal{A}$ is a given blurring operator, $\nabla\mathbf{u}=(\nabla_x\mathbf{u},\nabla_y\mathbf{u})$, λ and μ are positive parameters. With the fixed $\hat{\mathbf{P}}$ defined in (2.7), we let $\widetilde{\mathcal{A}}=\hat{\mathbf{P}}\mathcal{A}\hat{\mathbf{P}}^T$, $\widetilde{\mathbf{f}}=\hat{\mathbf{P}}\mathbf{f}$. We then reformulate the problem
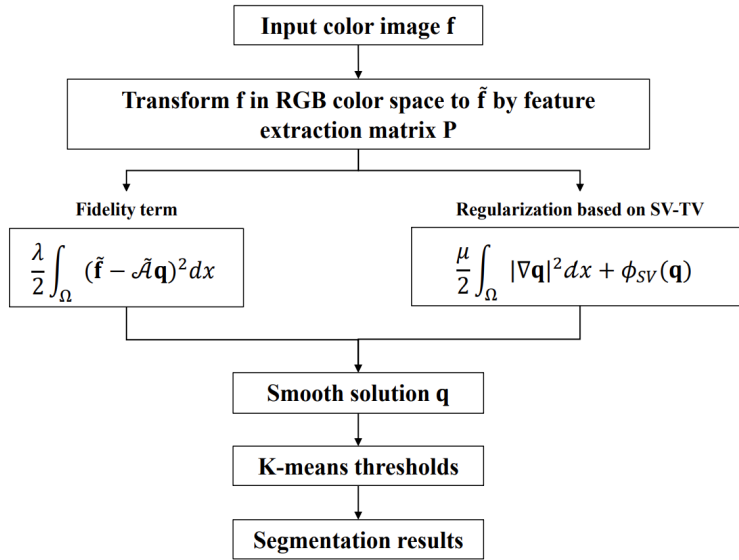

Figure 3: The flowchart of our method.

(3.1) as the following form

$$\min_{\mathbf{q}} \frac{\lambda}{2} \|\widetilde{\mathbf{f}} - \widetilde{\mathcal{A}}\mathbf{q}\|_2^2 + \frac{\mu}{2} \|\nabla\mathbf{q}\|_2^2 + \phi_{SV}(\mathbf{q}), \tag{3.2}$$

where

$$\phi_{SV}(\mathbf{q})$$
$$= \sum_{i=1}^{m}\sum_{j=1}^{n}\left(\sqrt{\sum_{k=1}^{2}(\nabla_x \mathbf{q}_k(i,j))^2 + (\nabla_y \mathbf{q}_k(i,j))^2} + \alpha\sqrt{(\nabla_x \mathbf{q}_3(i,j))^2 + (\nabla_y \mathbf{q}_3(i,j))^2}\right), \tag{3.3}$$

here $\alpha > 0$ is again the weight corresponding to the value component.

After $\mathbf{q}$ is obtained, the second stage is to threshold $\mathbf{q}$ directly to obtain our segmentation result before transforming it back to an RGB image with the matrix $\hat{\mathbf{P}}^T$. Many clustering method (the K-means method [27], the fuzzy C-means method [5], the convex K-means method [36], etc.) can be used to find the threshold to segment $\mathbf{q}$ into K phases ($K \geq 2$). In this paper, we use the MATLAB "*KMEANS*" command to implement our strategy of choosing thresholds automatically. The selection of thresholds and phases K is independent of the process of solving $\mathbf{q}$. That is, there is no need to recalculate $\mathbf{q}$ when changing thresholds or K and hence can reduce the runtime.

3.2 Algorithm

For the convex optimization problem (3.2), many algorithms are particularly adequate to solve it, such as the Douglas Rachford algorithm [47], the Chambolle Pock (CP) algorithm [13], the ADMM algorithm [21] and the proximal point algorithm [56]. In this paper, we use a first-order primal-dual algorithm introduced by Tran-Dinh et al. [48] with a guaranteed convergence rate. Unlike existing primal-dual schemes where the parameters are often fixed, this method adopts the pre-defined and dynamic sequences for parameters that can achieve a faster convergence rate.

In order to implement the primal-dual method, let

$$F(\mathbf{q}) = \frac{\lambda}{2}\|\widetilde{\mathbf{f}} - \widetilde{\mathcal{A}}\mathbf{q}\|_2^2, \quad G(\nabla\mathbf{q}) = \frac{\mu}{2}\|\nabla\mathbf{q}\|_2^2 + \text{SV-TV}(\mathbf{q}).$$

Note that G in fact depends on $\nabla\mathbf{q}$ only. To solve model (3.2), we first rewrite it into a min-max setting as follows:

$$\min_{\mathbf{q}}\max_{\mathbf{y}}\langle\nabla\mathbf{q},\mathbf{y}\rangle + F(\mathbf{q}) - G^*(\mathbf{y}), \tag{3.4}$$

where the conjugate function is defined as

$$G^*(\mathbf{y}) = \sup_{\mathbf{x}}\langle\mathbf{x},\mathbf{y}\rangle - G(\mathbf{x}).$$

Algorithm 3.1 New primal-dual algorithm to solve (3.4).

Initialization: Choose $q^0 = \widetilde{f}$, $y^0 \in \mathbb{Y}$, $\rho_0 > 0$, $c \geq 1$, and $\gamma \in (0,1)$.

1: $\tau_0 := 1$, $q^{-1} := \hat{q}^0 := q^0$, and $\tilde{q}^{-1} := \tilde{y}^0 := \bar{y}^0 := y^0$.

2: **for** $k := 0, 1, \cdots, k_{\max}$ **do**

3:     Update $\rho_k := \frac{\rho_0}{\tau_k}$, $\beta_k := \frac{\gamma}{\|\nabla\|^2 \rho_k}$, $\eta_k := (1-\gamma)\rho_k$, and $\tau_{k+1} := \frac{c}{k+c+1}$.

4:     Update the primal-dual step:

$$\begin{cases} y^{k+1} := \text{prox}_{\rho_k G^*}\left(\tilde{y}^k + \rho_k \nabla \hat{q}^k\right), & \text{solved by (3.10) and (3.11),} \\ q^{k+1} := \text{prox}_{\beta_k F}\left(\hat{q}^k - \beta_k \nabla^\top y^{k+1}\right), & \text{solved by (3.13),} \\ \hat{q}^{k+1} := q^{k+1} + \frac{\tau_{k+1}(1-\tau_k)}{\tau_k}\left(q^{k+1} - q^k\right). \end{cases}$$

5:     Update the intermediate dual step:

$$\tilde{y}^{k+1} := \tilde{y}^k + \eta_k \nabla\left[q^{k+1} - \hat{q}^k - (1-\tau_k)\left(q^k - \hat{q}^{k-1}\right)\right]$$
$$+ (1-\gamma)\left[y^{k+1} - \tilde{y}^k - \frac{\tau_{k-1}(1-\tau_k)}{\tau_k}\left(y^k - \tilde{y}^{k-1}\right)\right].$$

6:     Update the dual averaging step: $\bar{y}^{k+1} := (1-\tau_k)\bar{y}^k + \tau_k y^{k+1}$.

7: **end for**

Motivated by the primal-dual algorithm in [48], the algorithm for solving (3.4) is summarized in Algorithm 3.1. As introduced by Tran-Dinh et al. in [48], the parameters in Algorithm 3.1 are updated as follows:

$$\tau_k := \frac{c}{k+c}, \quad \rho_k := \frac{\rho_0}{\tau_k}, \quad \beta_k := \frac{\gamma}{\|\nabla\|^2 \rho_k} \quad \text{and} \quad \eta_k := (1-\gamma)\rho_k,$$

where $c \geq 1$, $\gamma \in (0,1)$, $\|\nabla\|^2 \leq 8$ and $\rho_0 > 0$ are given. The main computations of Algorithm 3.1 are the two proximal operators in Step 4. Next we elaborate on how to solve these subproblems respectively in Algorithm 3.1.

- **y-subproblem**

$$\mathbf{y}^{k+1} := \text{prox}_{\rho_k G^*}\left(\tilde{\mathbf{y}}^k + \rho_k \nabla \hat{\mathbf{q}}^k\right). \tag{3.5}$$

To derive the above proximal operator, we first calculate $G^*(\mathbf{y})$ by the definition of conjugate function. We denote $\mathbf{y} = (\mathbf{y_1}, \mathbf{y_2}, \mathbf{y_3})$, where $\mathbf{y_k} = (\mathbf{y_k^1}, \mathbf{y_k^2})$ for $k = 1, 2, 3$. Denote $\mathbf{y_*} = (\mathbf{y_1}, \mathbf{y_2})$ and thus $\mathbf{y} = (\mathbf{y_*}, \mathbf{y_3})$. To aid the presentation, we introduce the

following norms to $\mathbf{y}_*$ and $\mathbf{y_3}$

$$|\mathbf{y}_*(i,j)| = \sqrt{\left(\mathbf{y}_1^1(i,j)\right)^2 + \left(\mathbf{y}_1^2(i,j)\right)^2 + \left(\mathbf{y}_2^1(i,j)\right)^2 + \left(\mathbf{y}_2^2(i,j)\right)^2}, \qquad (3.6a)$$

$$|\mathbf{y_3}(i,j)| = \sqrt{\left(\mathbf{y}_3^1(i,j)\right)^2 + \left(\mathbf{y}_3^2(i,j)\right)^2}, \qquad (3.6b)$$

$$\|\mathbf{y}_*\|_\infty = \max_{i,j}|\mathbf{y}_*(i,j)|, \quad \|\mathbf{y_3}\|_\infty = \max_{i,j}|\mathbf{y_3}(i,j)|. \qquad (3.6c)$$

Note that G is separable with respect to each component of $\mathbf{y}$, i.e., $G(\mathbf{y}) = G_1(\mathbf{y}_*) + G_2(\mathbf{y_3})$. Given the definition of G, we have

$$G_1(\mathbf{y}_*) = \frac{\mu}{2}\|\mathbf{y}_*\|_2^2 + \|\mathbf{y}_*\|_1, \qquad (3.7)$$

$$G_2(\mathbf{y_3}) = \frac{\mu}{2}\|\mathbf{y_3}\|_2^2 + \alpha\|\mathbf{y_3}\|_1. \qquad (3.8)$$

We can then compute the conjugate function of G_1, G_2 separately. Thus the corresponding conjugate functions are

$$G_1^*(\mathbf{y}_*) = \frac{1}{2\mu}\|\mathbf{y}_* - \Pi_{P_1}(\mathbf{y}_*)\|_2^2, \qquad (3.9a)$$

$$G_2^*(\mathbf{y_3}) = \frac{1}{2\mu}\|\mathbf{y_3} - \Pi_{P_2}(\mathbf{y_3})\|_2^2, \qquad (3.9b)$$

where $\Pi_P(\cdot)$ denotes the projection onto a set P. Here

$$P_1 = \{\mathbf{y}_* : \|\mathbf{y}_*\|_\infty \le 1\}, \quad P_2 = \{\mathbf{y_3} : \|\mathbf{y_3}\|_\infty \le \alpha\}.$$

One can then derive the iteration of $\mathbf{y}^{k+1}$ by the definition of proximal operator

$$\mathrm{prox}_f(x) := \underset{y}{\arg\min}\left\{f(y) + \frac{1}{2}\|y - x\|^2\right\}.$$

By solving the corresponding quadratic problems, we get

$$\mathbf{y}_*^{k+1}(i,j) = \mathbf{x}_*^{\mathbf{k}}(i,j)\frac{\mu}{\mu + \rho_k} + \frac{\mathbf{x}_*^{\mathbf{k}}(i,j)}{\max\{1, |\mathbf{x}_*^{\mathbf{k}}(i,j)|\}}\frac{\rho_k}{\mu + \rho_k}, \qquad (3.10)$$

where $\mathbf{x}_*^{\mathbf{k}}(i,j) = (\tilde{\mathbf{y}}_*^k + \rho_k \nabla \hat{\mathbf{q}}_*^k)(i,j)$, $\mathbf{q}_* = (\mathbf{q_1}, \mathbf{q_2})$, and

$$\mathbf{y_3}^{k+1}(i,j) = \mathbf{x_3}^{\mathbf{k}}(i,j)\frac{\mu}{\mu + \rho_k} + \frac{\mathbf{x_3}^{\mathbf{k}}(i,j)}{\max\{\alpha, |\mathbf{x_3}^{\mathbf{k}}(i,j)|\}}\frac{\alpha\rho_k}{\mu + \rho_k}, \qquad (3.11)$$

where $\mathbf{x_3}^{\mathbf{k}}(i,j) = (\tilde{\mathbf{y_3}}^k + \rho_k \nabla \hat{\mathbf{q_3}}^k)(i,j)$.

- **q**-subproblem

$$\mathbf{q}^{k+1} = \text{prox}_{\beta_k F}\left(\hat{\mathbf{q}}^k - \beta_k \nabla^\top \mathbf{y}^{k+1}\right)$$
$$= \underset{\mathbf{q}}{\arg\min} \frac{\beta\lambda}{2}\|\widetilde{\mathbf{f}} - \widetilde{\mathcal{A}}\mathbf{q}\|_2^2 + \frac{1}{2}\|\mathbf{q} - (\hat{\mathbf{q}}^k - \beta_k\nabla^\top\mathbf{y}^{k+1})\|_2^2. \qquad (3.12)$$

The above problem is a quadratic problem and can be solved analytically as follows:

$$\mathbf{q}^{k+1} = (\beta_k\lambda\mathcal{A}^\top\mathcal{A} + I)^{-1}(\hat{\mathbf{q}}^k - \beta_k\nabla^\top\mathbf{y}^{k+1} + \beta_k\lambda\widetilde{\mathbf{f}}). \qquad (3.13)$$

4 Experimental results

To demonstrate the effectiveness of our two-stage segmentation method based on saturation-value total variation, we present the numerical and visual results in this section. We compare the proposed method with some state-of-the-art approaches (FP [46], SLat [9], SFFCM [31], RSSFCA [28], AFCF [32]). Method [46] uses an ADMM algorithm to solve the piecewise constant Mumford-Shah model with structured Potts priors. Method [31] uses a fast super-pixel method to pre-process the image before clustering to improve the efficiency and stability of the segmentation. Method [28,32] are two different clustering methods that have low memory demand but high performance. Method [9] converts the RGB color image into the Lab color space before thresholding to obtain more image information, thus improving the accuracy of segmentation. These methods were originally designed to work on color images. All the codes are provided by the authors and the parameters in the codes are chosen empirically to give the best results of each method. For our model (3.2), we fix $\mu = 1$, $\lambda = 3$, $\alpha = 1$.

All experiments are performed via MATLAB R2018a and Windows 10($\times$64) on a PC with Intel Core(TM) i5-8250U CPU 1.60GHz and 8.0GB memory. We present the tests on the real-world color images given in Fig. 4 (all images are chosen from the Berkeley Segmentation Dataset 300). We take three different forms of image degradation into account: noise, blur, and information loss. The Gaussian noise are all generated using the MATLAB function "*imnoise*", with mean 0 and variance 0.001 or 0.01. The blurring kernels were all obtained by horizontal motion-blur with 10 pixels length. For the information loss case, we deleted 40% pixel values randomly. In Stage 1 of our method, the primal-dual Algorithm 3.1 is adopted to solve the model (3.2) and the maximum iteration number is set as 100. In stage 2, given the number of phases K, the thresholds are calculated automatically by the MATLAB K-means function "*KMEANS*".

4.1 The primal-dual algorithm vs the ADMM algorithm

To illustrate the effectiveness of the new primal-dual algorithm, we compare it with the widely used ADMM algorithm, using these two algorithms to solve (3.2). In Fig. 5, we

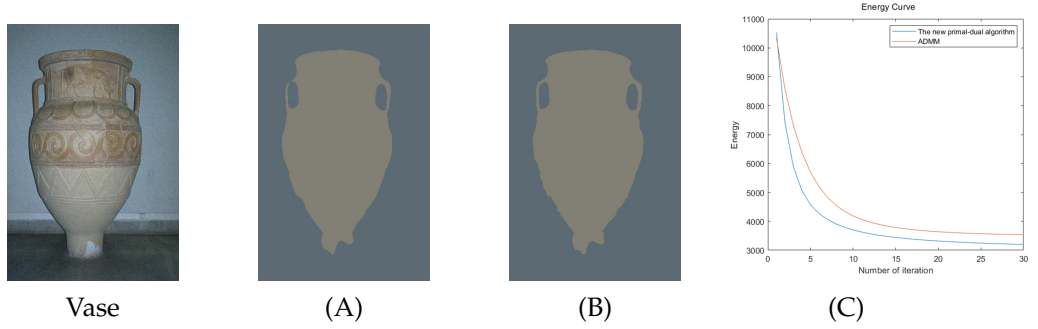Figure 4: Real-world test images used in our experiment. All images are chosen from BSD300.

Figure 5: The Segmentation results of different algorithm on "Vase". (A): Result of ADMM; (B): Result of the new primal-dual algorithm; (C): Energy plots of ADMM and the new primal-dual algorithm.

show the energy graph for the test image "Vase" with Gaussian noise 0.001 added. We observe that the energy under the new primal-dual algorithm drops to around 3200 within 30 iterations which is faster than ADMM. The segmentation results of ADMM and the new primal-dual algorithm are shown in Fig. 5. From the results, the segmentation effect of the new primal-dual algorithm is better than that of ADMM for the same number of iterations, which also shows that our model is effective.

4.2 Effectiveness of regularization terms

In this subsection, we present an ablation study to demonstrate the effectiveness of the regularization terms in (3.2). More specifically, We compare the following models:

$$\text{Model 1:} \qquad \arg\min_{\mathbf{q}} \frac{\lambda}{2}\|\widetilde{\mathbf{f}}-\widetilde{\mathcal{A}}\mathbf{q}\|_2^2+\phi_{SV}(\mathbf{q}), \qquad (4.1a)$$

$$\text{Model 2:} \qquad \arg\min_{\mathbf{q}} \frac{\lambda}{2}\|\widetilde{\mathbf{f}} - \widetilde{\mathcal{A}}\mathbf{q}\|_2^2 + \frac{\mu}{2}\|\nabla\mathbf{q}\|_2^2, \qquad (4.1b)$$

$$\text{Proposed:} \qquad \arg\min_{\mathbf{q}} \frac{\lambda}{2}\|\widetilde{\mathbf{f}} - \widetilde{\mathcal{A}}\mathbf{q}\|_2^2 + \frac{\mu}{2}\|\nabla\mathbf{q}\|_2^2 + \phi_{SV}(\mathbf{q}). \qquad (4.1c)$$

For this experiment, we select the image "Island" as the test image. We set the number of phases K to be 2. The results of the compared models are shown in Fig. 6. As shown in the figure, part of the corners of the image is segmented in the result of Model 1. Without the squared gradient term, the intermediate result from stage 1 is not sufficiently smoothed and hence leads to this inaccurate segmentation result. As for Model 2, without the SV-TV term, the saturation and brightness information is not incorporated. Therefore, the foreground and background are not properly distinguished. On the contrary, with both regularization terms, the proposed model successfully performs the task, showcasing the effectiveness of both the regularization terms.
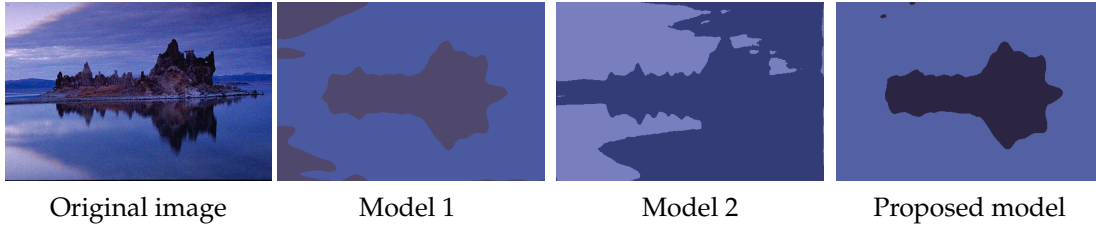

| Original image | Model 1 | Model 2 | Proposed model |

Figure 6: Ablation study of the effect of the regularization terms.

4.3 Number of clusters

Most segmentation models require us to determine the number of clusters K in advance, but the selection of phases K often has a great impact on the segmentation results. We first study the effect of the choice of K on the compared methods and our method. We test on the images "Vase", "Island" and "Bird". We report the segmentation results with $K=2,3$ of the compared methods and our method in Figs. 7–9.

As shown in Fig. 7, when we choose $K=3$, most methods can separate the vase from the background, but when we take $K=2$, a more intuitive choice, other methods do not perform the segmentation task well. The reason for the poor segmentation when $K=2$ is that the color of the vase and the background are relatively similar, which may lead to confusion when sorting by color only. Our method also takes into account the saturation and brightness information, which is important to distinguish the foreground and the background of the image, so we can accurately segment the vase at different values of K. The same situation happens for the test image "Island" in Fig. 8, where the value of K has a large impact on the other methods because the color of the island and the background are too close to each other. Our method is also effective in classifying multiple targets. For example, as shown in Fig. 9, we can segment the foreground and the background
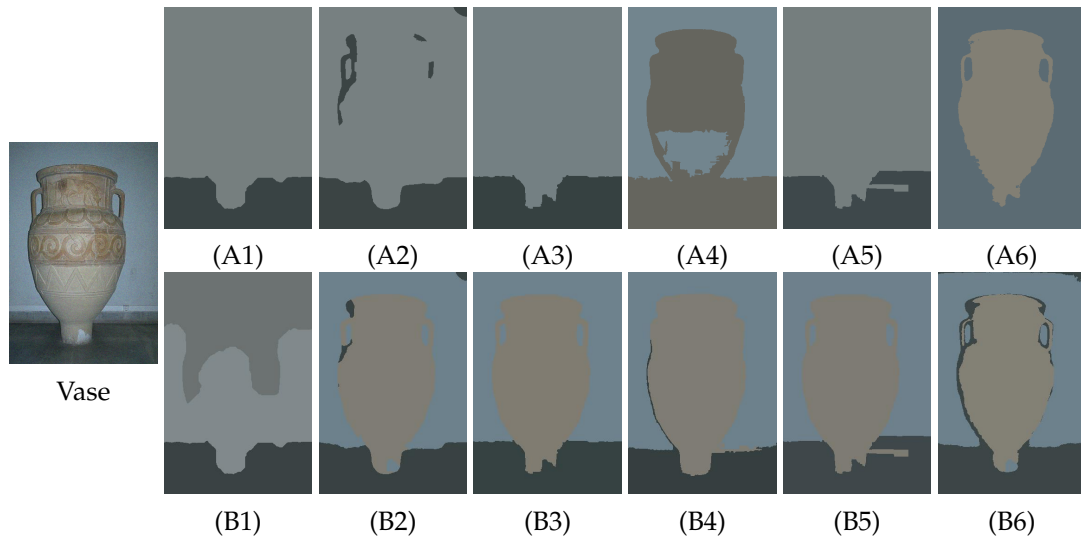
Figure 7: Segmentation at different phases K. (A1)-(A6) and (B1)-(B6): Results of methods [9, 28, 31, 32, 46] and ours when $K=2$ and $K=3$ respectively.
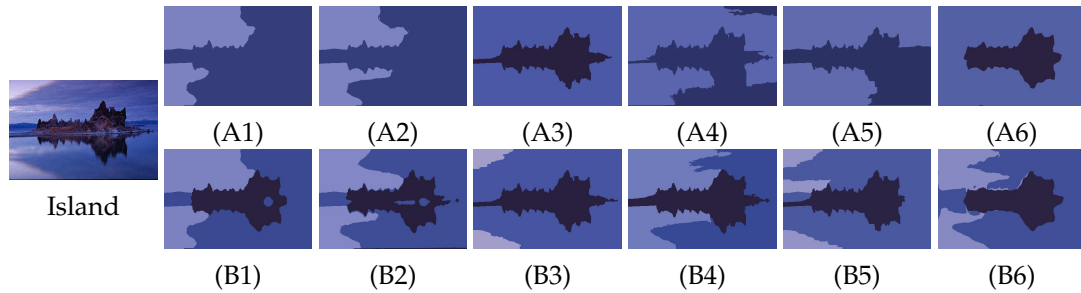

Figure 8: Segmentation at different phases K. (A1)-(A6) and (B1)-(B6): Results of methods [9, 28, 31, 32, 46] and ours when $K=2$ and $K=3$ respectively.

well at $K=2$, and further segment the bird and the tree accurately at $K=3$, while other methods cannot achieve such accuracy. Due to the use of SV-TV, our method combines the features of the image in both RGB and HSV spaces when doing segmentation, thus our method is very robust and accurate at different values of K.

4.4 Numerical results

In this experiment, we compare our method with five excellent methods (FP [46], SLat [9], SFFCM [31], RSSFCA [28], AFCF [32]). We compare the methods on 10 real-world color images for both two-phase and multi-phase segmentation. We consider three cases for each test image: images with a slight noise, motion blurred images with higher noise, and images with information loss. The segmentation results are shown in Figs. 10-19. We
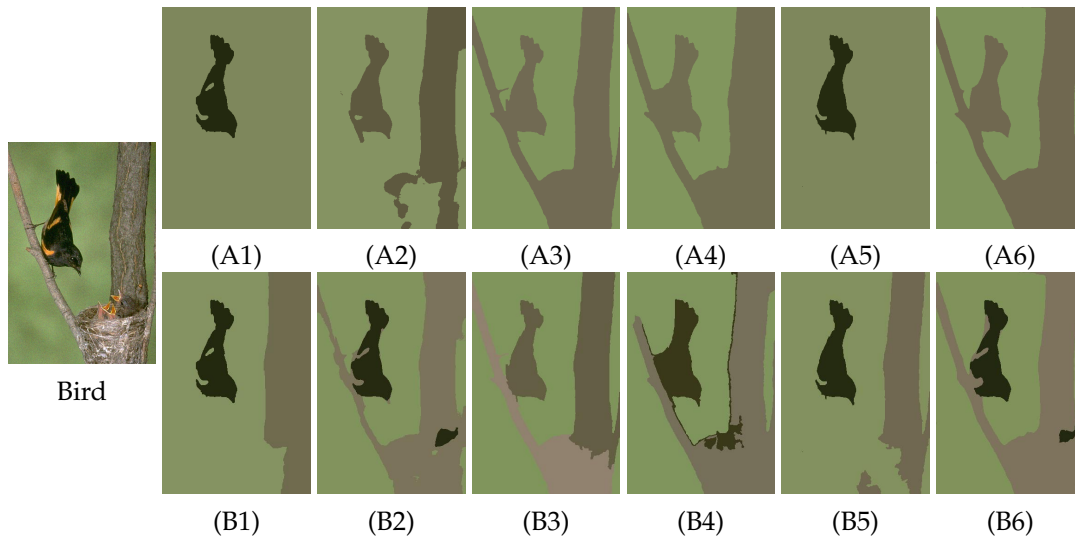
Figure 9: Segmentation at different phases K. (A1)-(A6) and (B1)-(B6): Results of methods $[9, 28, 31, 32, 46]$ and ours when $K=2$ and $K=3$ respectively.
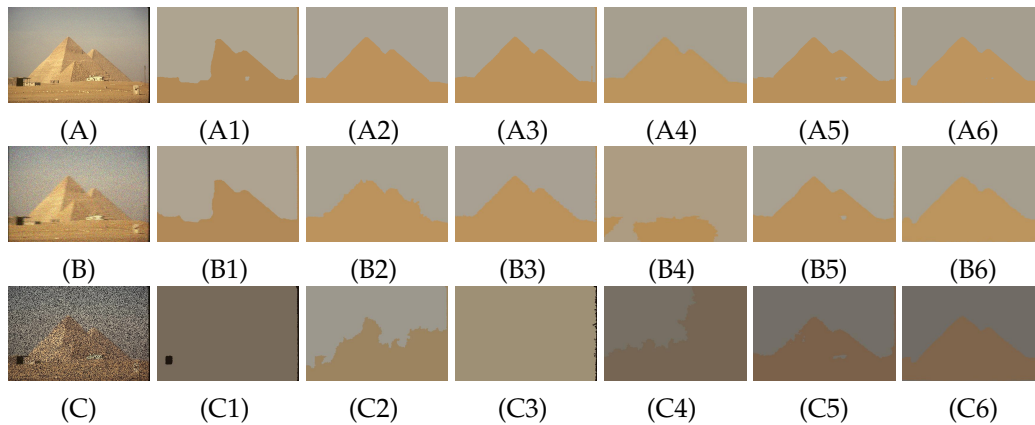

Figure 10: Two-phase pyramid segmentation. (A): Given Gaussian noisy image with mean 0 and noise 0.001; (B):Given blurry image with Gaussian noise. (C):Given image with 40% information loss; (A1)-(A6), (B1)-(B6) and (C1)-(C6): Corresponding results of methods $[9, 28, 31, 32, 46]$ and ours in the corresponding cases.

can see from the figures that our method outperforms other competing methods in most cases, and our results are consistent with the human visual segmentation. In the case of images with a slight noise, most methods can achieve good segmentation results when the object is originally well separated from the background. However, in the latter two cases, the results of the other methods show varying degrees of degradation, especially for the case of missing pixels, where some methods completely fail to segment the target object. This suggests that higher noise level, blurring, and missing pixels all have a sig-
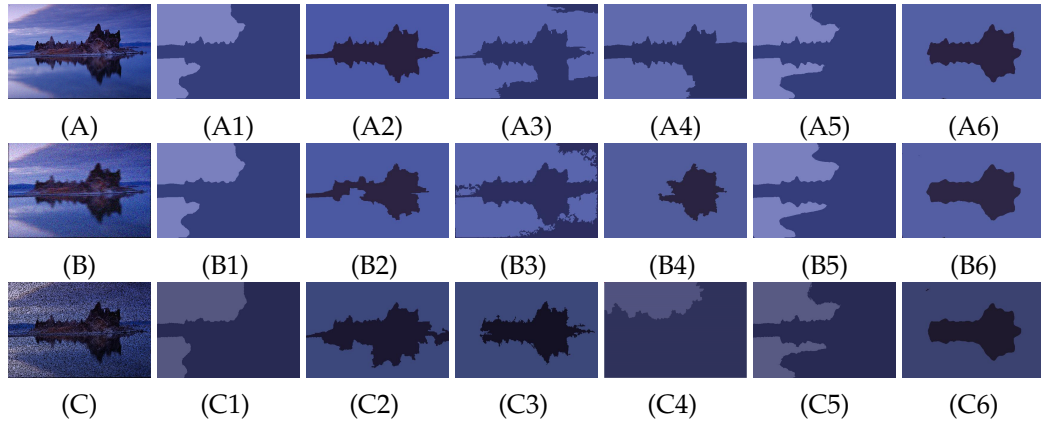
Figure 11: Two-phase island segmentation. (A): Given Gaussian noisy image with mean 0 and noise 0.001; (B):Given blurry image with Gaussian noise. (C):Given image with 40% information loss; (A1)-(A6), (B1)-(B6) and (C1)-(C6): Results of methods $[9, 28, 31, 32, 46]$ and ours in the corresponding cases.
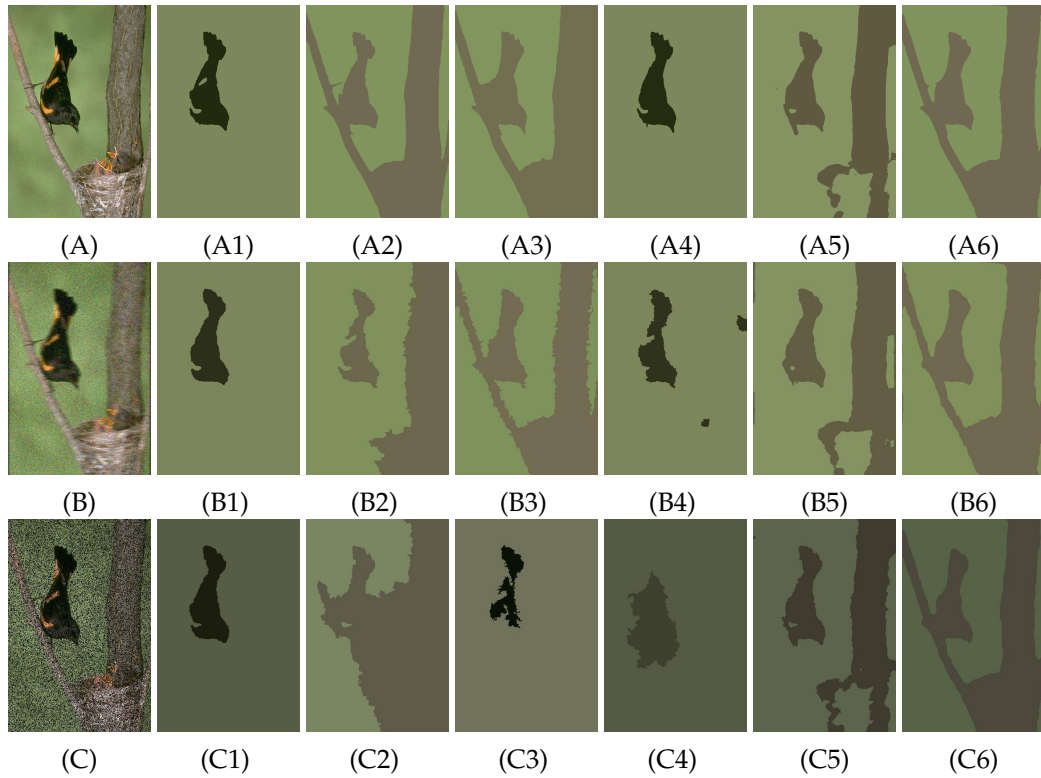

Figure 12: Two-phase bird segmentation. (A): Given Gaussian noisy image with mean 0 and noise 0.001; (B):Given blurry image with Gaussian noise. (C):Given image with 40% information loss; (A1)-(A6), (B1)-(B6) and (C1)-(C6): Results of methods $[9, 28, 31, 32, 46]$ and ours in the corresponding cases.
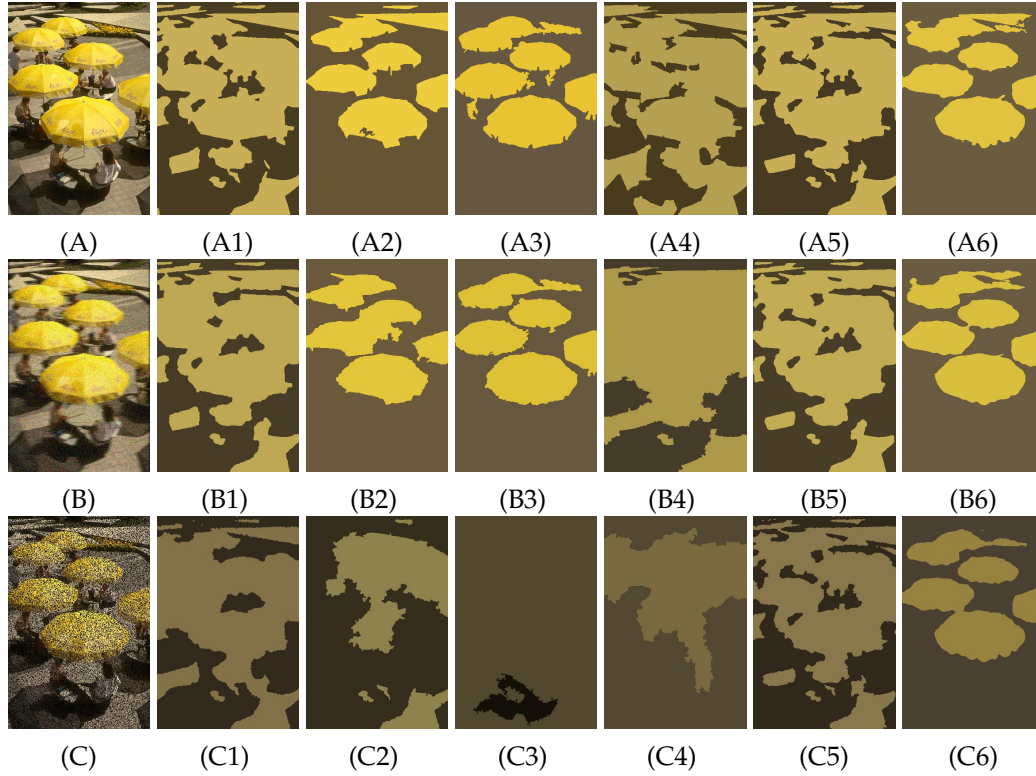
Figure 13: Two-phase umbrella segmentation. (A): Given Gaussian noisy image with mean 0 and noise 0.001; (B):Given blurry image with Gaussian noise. (C):Given image with 40% information loss; (A1)-(A6), (B1)-(B6) and (C1)-(C6): Results of methods [9, 28, 31, 32, 46] and ours in the corresponding cases.

nificant impact on most segmentation models. On the other hand, from the experimental results, our method still maintains good segmentation results in these cases of degraded images, which is mainly attributed to the good image recovery of our first stage. While most methods in the RGB space do not work well when the color of the object is similar to the background color, our method shows good performance due to the use of the SV-TV regularization in the HSV color space, which can extract the saturation and brightness information of an image. Furthermore, the CPU time of the methods given in Table 1 shows that our method is the most efficient among variational-based methods.

5   Conclusions

In this paper, we proposed a two-stage color image segmentation method based on SV-TV regularization. And the SV-TV is constructed by the quaternion-based method which takes the relationship among RGB channels into account. At the first stage, we find a smooth approximation $\mathbf{q}$ of the P-transformed RGB image, and the minimization prob-
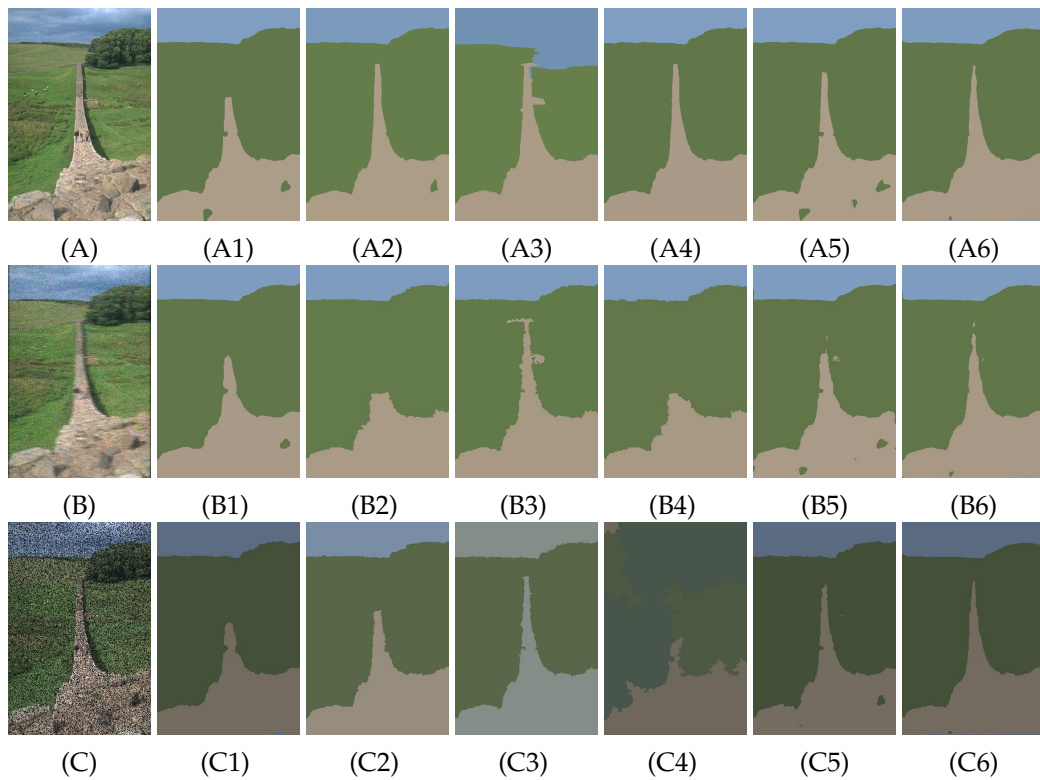
Figure 14: Three-phase path segmentation. (A): Given Gaussian noisy image with mean 0 and noise 0.001; (B): Given blurry image with Gaussian noise. (C): Given image with 40% information loss; (A1)-(A6), (B1)-(B6) and (C1)-(C6): Results of methods [9, 28, 31, 32, 46] and ours in the corresponding cases.
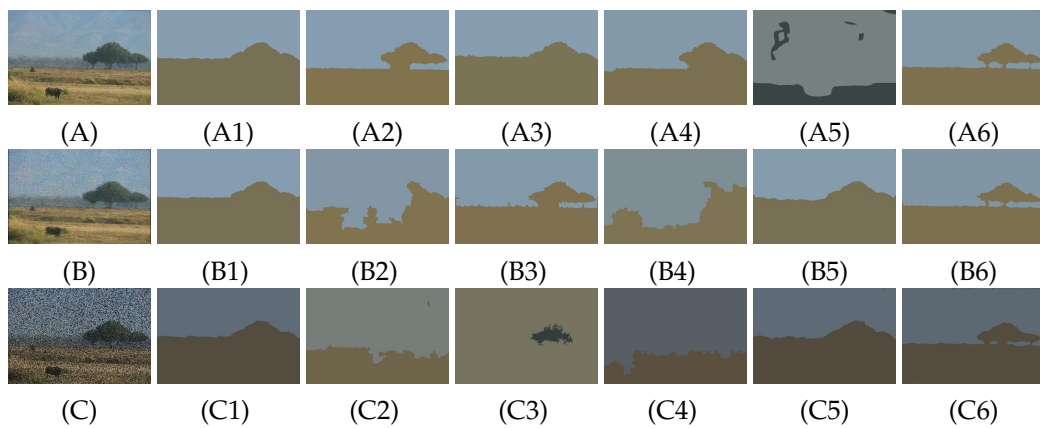

Figure 15: Two-phase grassland segmentation. (A): Given Gaussian noisy image with mean 0 and noise 0.001; (B): Given blurry image with Gaussian noise. (C):Given image with 40% information loss; (A1)-(A6), (B1)-(B6) and (C1)-(C6): Results of methods [9, 28, 31, 32, 46] and ours in the corresponding cases.
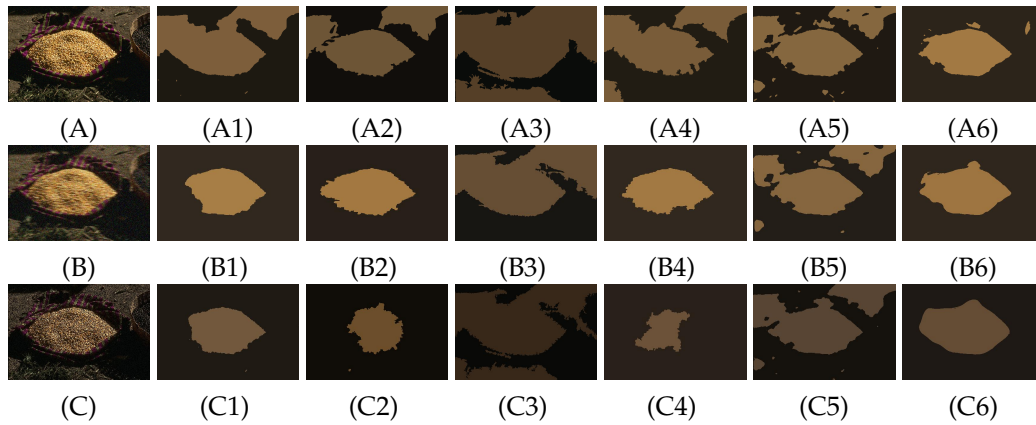
Figure 16: Two-phase grassland segmentation. (A): Given Gaussian noisy image with mean 0 and noise 0.001; (B):Given blurry image with Gaussian noise. (C):Given image with 40% information loss; (A1)-(A6), (B1)-(B6) and (C1)-(C6): Results of methods $[9, 28, 31, 32, 46]$ and ours in the corresponding cases.

Figure 17: Three-phase koala segmentation. (A): Given Gaussian noisy image with mean 0 and noise 0.001; (B):Given blurry image with Gaussian noise. (C):Given image with 40% information loss; (A1)-(A6), (B1)-(B6) and (C1)-(C6): Results of methods $[9, 28, 31, 32, 46]$ and ours in the corresponding cases.

Figure 18: Three-phase man segmentation. (A): Given Gaussian noisy image with mean 0 and noise 0.001; (B):Given blurry image with Gaussian noise. (C):Given image with 40% information loss; (A1)-(A6), (B1)-(B6) and (C1)-(C6): Results of methods $[9, 28, 31, 32, 46]$ and ours in the corresponding cases.
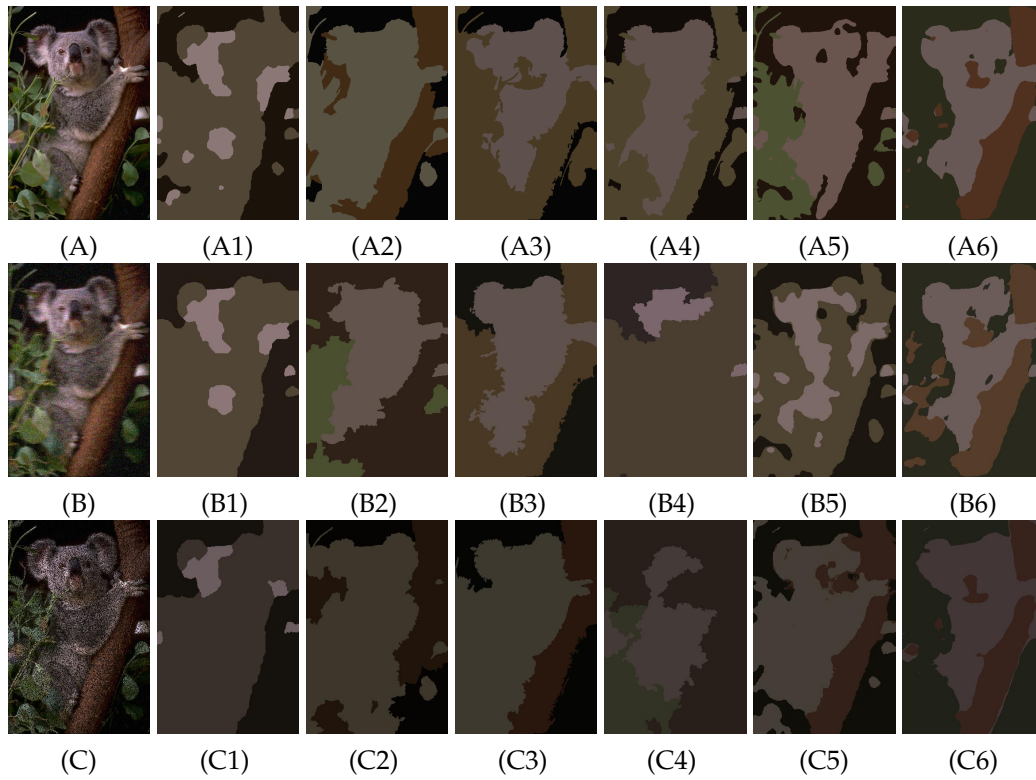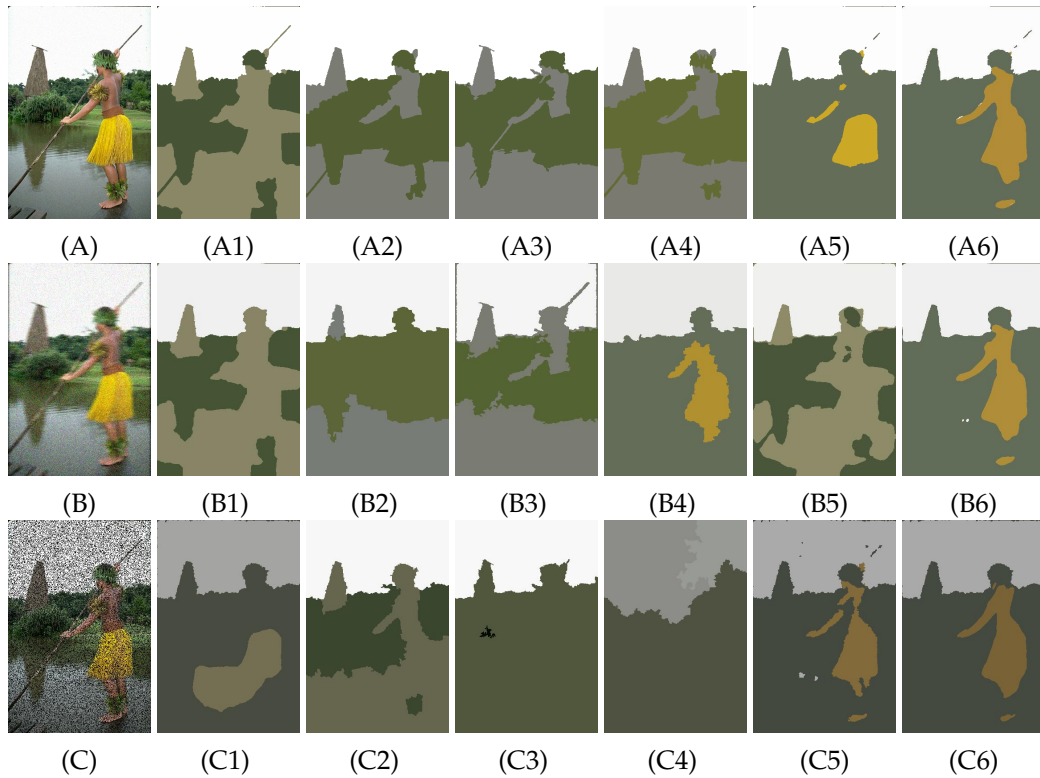
lem is designed to be solved by a new primal-dual algorithm with guaranteed convergence. Then the segmentation results can be obtained by thresholding in the second

Table 1: The CPU time of methods $[9, 28, 31, 32, 46]$ and ours in seconds.

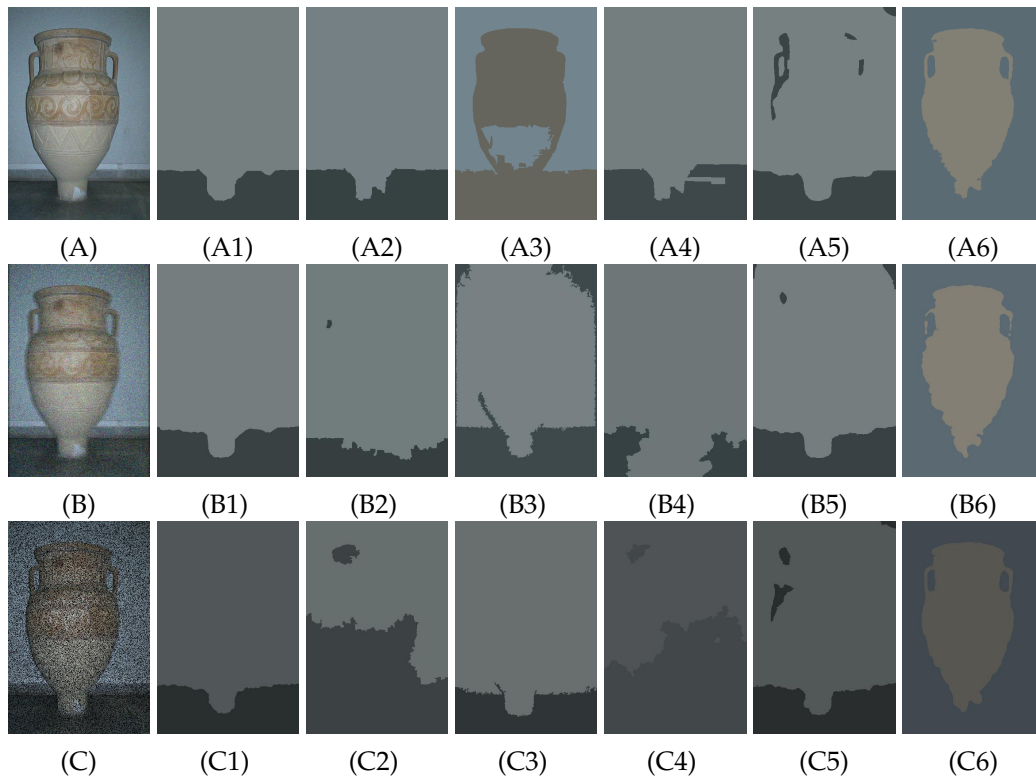| Methods	Clustering methods			Variational-based methods		
	Method [32]	Method [31]	Method [28]	Method [46]	Method [9]	Ours
Pyramid	2.32	1.69	49.42	6.54	10.08	6.13
Island	2.86	1.82	46.64	7.06	16.61	6.29
Bird	2.65	1.77	49.56	9.53	14.20	6.21
Umbrella	2.94	2.32	46.37	7.13	16.66	6.34
Path	2.48	1.86	49.96	6.77	13.31	5.97
Grassland	2.36	1.75	47.77	5.68	16.57	5.62
Corn	2.41	2.13	48.57	6.87	19.95	6.12
Koala	2.67	1.98	47.25	7.78	20.77	6.68
Man	2.57	1.77	47.78	6.25	12.17	6.09
Vase	2.34	1.97	48.37	6.73	15.18	6.31

Figure 19: Two-phase vase segmentation. (A): Given Gaussian noisy image with mean 0 and noise 0.001; (B):Given blurry image with Gaussian noise. (C):Given image with 40% information loss; (A1)-(A6), (B1)-(B6) and (C1)-(C6): Results of methods [9, 28, 31, 32, 46] and ours in the corresponding cases.

stage. The new two-stage method has the ability to segment images corrupted by noise, blur, or pixel information loss. Experimental results demonstrate that our method gives much better segmentation results for images with degradation than some state-of-the-art segmentation models both in terms of quality and stability. Further research on the regularization which describes the intrinsic connection among multiple channels would be concerned in the future.

References

[1] L. AMBROSIO AND T. V. M., *On the approximation of free discontinuity problems*, Bollettino della Unione Matematica Italiana B, 7 (1992), pp. 1–20.

[2] L. AMBROSIO AND T. V. MARIA, *Approximation of functional depending on jumps by elliptic functional via t-convergence*, Commun. Pure Appl. Math., 43 (1990), pp. 999–1036.

[3] E. BAE, J. YUAN, AND X. C. TAI, *Simultaneous convex optimization of regions and region parameters in image segmentation models*, Innovations for Shape Analysis, Springer, 2013, pp. 421–438.

[4] H. BENNINGHOFF AND H. GARCKE, *Efficient image segmentation and restoration using parametric curve evolution with junctions and topology changes*, SIAM J. Imag. Sci., 7 (2014), pp. 1451–1483.

[5] J. C. BEZDEK, R. EHRLICH, AND W. FULL, *Fcm: The fuzzy c-means clustering algorithm*, Comput. Geosci., 10 (1984), pp. 191–203.

[6] X. BRESSON, S. ESEDOGLU, P. VANDERGHEYNST, J. P. THIRAN, AND S. OSHER, *Fast global minimization of the active contour/snake model*, J. Math. Imag. Vision, 28 (2007), pp. 151–167.

[7] E. S. BROWN, T. F. CHAN, AND X. BRESSON, *Completely convex formulation of the Chan-Vese image segmentation model*, Int. J. Comput. Vision, 98 (2012), pp. 103–121.

[8] X. CAI, *Variational image segmentation model coupled with image restoration achievements*, Pattern Recognition, 48 (2015), pp. 2029–2042.

[9] X. CAI, R. CHAN, M. NIKOLOVA, AND T. ZENG, *A three-stage approach for segmenting degraded color images: Smoothing, lifting and thresholding (SLaT)*, J. Sci. Comput., 72 (2017), pp. 1313–1332.

[10] X. CAI, R. CHAN, AND T. ZENG, *A two-stage image segmentation method using a convex variant of the Mumford–Shah model and thresholding*, SIAM J. Imag. Sci., 6 (2013), pp. 368–390.

[11] A. CHAMBOLLE, *Finite-differences discretizations of the Mumford-Shah functional*, ESAIM: Math. Model. Numer. Anal., 33 (1999), pp. 261–288.

[12] A. CHAMBOLLE AND G. DAL MASO, *Discrete approximation of the Mumford-Shah functional in dimension two*, ESAIM: Math. Model. Numer. Anal., 33 (1999), pp. 651–672.

[13] A. CHAMBOLLE AND T. POCK, *A first-order primal-dual algorithm for convex problems with applications to imaging*, J. Math. Imag. Vision, 40 (2011), pp. 120–145.

[14] R. CHAN, H. YANG, AND T. ZENG, *A two-stage image segmentation method for blurry images with poisson or multiplicative gamma noise*, SIAM J. Imag. Sci., 7 (2014), pp. 98–127.

[15] T. F. CHAN, S. ESEDOGLU, AND M. NIKOLOVA, *Algorithms for finding global minimizers of image segmentation and denoising models*, SIAM J. Appl. Math., 66 (2006), pp. 1632–1648.

[16] T. F. CHAN AND L. A. VESE, *Active contours without edges*, IEEE Transactions on Image Processing, 10 (2001), pp. 266–277.

[17] Y. CHEN, Z. JIA, Y. PENG, AND Y. PENG, *Robust dual-color watermarking based on quaternion singular value decomposition*, IEEE Access, 8 (2020), pp. 30628–30642.

[18] Y. CHEN, X. XIAO, AND Y. ZHOU, *Low-rank quaternion approximation for color image processing*, IEEE Transactions on Image Processing, 29 (2019), pp. 1426–1439.

[19] P. DENIS, P. CARRÉ, AND C. FERNANDEZ-MALOIGNE, *Spatial and spectral quaternionic approaches for colour images*, Computer Vision and Image Understanding, 107 (2007), pp. 74–87.

[20] Y. DUAN, W. HUANG, J. ZHOU, H. CHANG, AND T. ZENG, *A two-stage image segmentation method using Euler's elastica regularized Mumford-Shah model*, 2014 22nd International Conference on Pattern Recognition, IEEE, 2014, pp. 118–123.

[21] J. ECKSTEIN AND W. YAO, *Approximate ADMM algorithms derived from Lagrangian splitting*, Comput. Optim. Appl., 68 (2017), pp. 363–405.

[22] S. ESEDOG, Y.-H. R. TSAI, ET AL., *Threshold dynamics for the piecewise constant Mumford–Shah functional*, J. Comput. Phys., 211 (2006), pp. 367–384.

[23] V. FERRARI, T. TUYTELAARS, AND L. VAN GOOL, *Object detection by contour segment networks*, European Conference on Computer Vision, Springer, 2006, pp. 14–28.

[24] M. FOARE, N. PUSTELNIK, AND L. CONDAT, *Semi-linearized proximal alternating minimization for a discrete Mumford–Shah model*, IEEE Transactions on Image Processing, 29 (2019), pp. 2176–2189.

[25] M. GOBBINO, *Finite difference approximation of the Mumford-Shah functional*, Communications

on Pure and Applied Mathematics: A Journal Issued by the Courant Institute of Mathematical Sciences, 51 (1998), pp. 197–228.

[26] W. R. HAMILTON, *Elements of quaternions*, London: Longmans, Green, & Company, 1866.

[27] J. A. HARTIGAN AND M. A. WONG, *Algorithm as 136: A k-means clustering algorithm*, Journal of the Royal Statistical Society. Series C, (Applied Statistics), 28 (1979), pp. 100–108.

[28] X. JIA, T. LEI, X. DU, S. LIU, H. MENG, AND A. K. NANDI, *Robust self-sparse fuzzy clustering for image segmentation*, IEEE Access, 8 (2020), pp. 146182–146195.

[29] Z. JIA, M. K. NG, AND W. WANG, *Color image restoration by saturation-value total variation*, SIAM J. Imag. Sci., 12 (2019), pp. 972–1000.

[30] D. A. KAY AND A. TOMASI, *Color image segmentation by the vector-valued allen–cahn phase-field model: a multigrid solution*, IEEE Transactions on Image Processing, 18 (2009), pp. 2330–2339.

[31] T. LEI, X. JIA, Y. ZHANG, S. LIU, H. MENG, AND A. K. NANDI, *Superpixel-based fast fuzzy c-means clustering for color image segmentation*, IEEE Transactions on Fuzzy Systems, 27 (2018), pp. 1753–1766.

[32] T. LEI, P. LIU, X. JIA, X. ZHANG, H. MENG, AND A. K. NANDI, *Automatic fuzzy clustering framework for image segmentation*, IEEE Transactions on Fuzzy Systems, 28 (2019), pp. 2078–2092.

[33] F. LI, M. K. NG, T. Y. ZENG, AND C. SHEN, *A multiphase image segmentation method based on fuzzy region competition*, SIAM J. Imag. Sci., 3 (2010), pp. 277–299.

[34] Z. LI AND T. ZENG, *A two-stage image segmentation model for multi-channel images*, Commun. Comput. Phys., 19 (2016), pp. 904–926.

[35] J. LIE, M. LYSAKER, AND X.-C. TAI, *A binary level set model and some applications to Mumford-Shah image segmentation*, IEEE Transactions on Image Processing, 15 (2006), pp. 1171–1181.

[36] F. LINDSTEN, H. OHLSSON, AND L. LJUNG, *Just relax and come clustering!: A convexification of k-means clustering*, Linköping University Electronic Press, 2011.

[37] C. LIU, M. K.-P. NG, AND T. ZENG, *Weighted variational model for selective image segmentation with application to medical images*, Pattern Recognition, 76 (2018), pp. 367–379.

[38] M. MORINI AND M. NEGRI, *Mumford–Shah functional as γ-limit of discrete Perona–Malik energies*, Math. Models Methods Appl. Sci., 13 (2003), pp. 785–805.

[39] D. MUMFORD AND J. SHAH, *Boundary detection by minimizing functionals*, IEEE Conference on Computer Vision and Pattern Recognition, vol. 17, San Francisco, 1985, pp. 137–154.

[40] D. B. MUMFORD AND J. SHAH, *Optimal approximations by piecewise smooth functions and associated variational problems*, Commun. pure Appl. Math., (1989).

[41] J. NÚNEZ AND J. LLACER, *Astronomical image segmentation by self-organizing neural networks and wavelets*, Neural Networks, 16 (2003), pp. 411–417.

[42] T. POCK, C. ANTONIN, C. DANIEL, AND H. BISCHOF, *A convex relaxation approach for computing minimal partitions*, 2009 IEEE Conference on Computer Vision and Pattern Recognition, IEEE, 2009, pp. 810–817.

[43] T. POCK, A. CHAMBOLLE, D. CREMERS, AND H. BISCHOF, *A convex relaxation approach for computing minimal partitions*, in 2009 IEEE Conference on Computer Vision and Pattern Recognition, IEEE, 2009, pp. 810–817.

[44] O. RONNEBERGER, P. FISCHER, AND T. BROX, *U-net: Convolutional networks for biomedical image segmentation*, International Conference on Medical Image Computing and Computer-Assisted Intervention, Springer, 2015, pp. 234–241.

[45] C. ROTARU, T. GRAF, AND J. ZHANG, *Color image segmentation in HSI space for automotive applications*, J. Real-Time Image Process., 3 (2008), pp. 311–322.

[46] M. STORATH AND A. WEINMANN, *Fast partitioning of vector-valued images*, SIAM J. Imag.

Sci., 7 (2014), pp. 1826–1852.

[47] B. F. SVAITER, *On weak convergence of the Douglas–Rachford method*, SIAM J. Control Optim., 49 (2011), pp. 280–287.

[48] Q. TRAN-DINH AND Y. ZHU, *Non-stationary first-order primal-dual algorithms with faster convergence rates*, SIAM J. Optim., 30 (2020), pp. 2866–2896.

[49] D. WANG AND X.-P. WANG, *The iterative convolution-thresholding method (ICTM) for image segmentation*, arXiv preprint, arXiv:1904.10917, (2019).

[50] H. WEI, C. YANG, AND Q. YU, *Contour segment grouping for object detection*, Journal of Visual Communication and Image Representation, 48 (2017), pp. 292–309.

[51] T. WU AND J. SHAO, *Non-convex and convex coupling image segmentation via tgpv regularization and thresholding*, Adv. Appl. Math. Mech., 12 (2020), pp. 849–878.

[52] Y. XU, L. YU, H. XU, H. ZHANG, AND T. NGUYEN, *Vector sparse representation of color image using quaternion matrix analysis*, IEEE Transactions on Image Processing, 24 (2015), pp. 1315–1329.

[53] Y. YU, Y. ZHANG, AND S. YUAN, *Quaternion-based weighted nuclear norm minimization for color image denoising*, Neurocomputing, 332 (2019), pp. 283–297.

[54] J. YUAN, E. BAE, X. C. TAI, AND Y. BOYKOV, *A continuous max-flow approach to potts model*, in European Conference on Computer Vision, Springer, 2010, pp. 379–392.

[55] M. ZHAO, Z. JIA, AND D. GONG, *Improved two-dimensional quaternion principal component analysis*, IEEE Access, 7 (2019), pp. 79409–79417.

[56] W. ZHU, S. SHU, AND L. CHENG, *An efficient proximity point algorithm for total-variation-based image restoration*, Adv. Appl. Math. Mech., 6 (2014), pp. 145–164.